Invited Review

Extended X-ray Absorption Fine Structure: A Modern Structural Tool in Materials Science

JOE WONG

UNIVERSITY OF CALIFORNIA
LAWRENCE LIVERMORE NATIONAL LABORATORY   P.O. BOX 808
(Received December 19, 1985)   LIVERMORE, CALIFORNIA 94550

ABSTRACT

Added to the structural tool-box of materials scientists, chemists, biologists, physicists and other scientists alike is an X-ray absorption technique, better known by its modern name as extended X-ray absorption fine structure (EXAFS). This technique has now been established to be a very powerful and sometimes unique way of probing the local atomic structure of all forms of matter, particularly since the availability of highly intense synchrotron radiation in the X-ray region. The unique features of EXAFS are (a) that it is element selective, (b) that it has a high sensitivity to short-range order in furnishing bond distance, coordination number and chemical identity of nearest neighbors and (c) that it is applicable to all states of matter in bulk and dilute forms, the latter including surfaces and adsorbates. The nature of the bonding about the X-ray absorbing atom may also be determined from the so-called near-edge structure within about 30 eV of the corresponding X-ray absorption edge. In this review the physical mechanism associated with the EXAFS phenomenon is presented in the light of the single-scattering formalism. The use of synchrotron radiation as a light source for EXAFS experiments and the use of data analysis to extract quantitative structural information are discussed by way of examples. A number of authoritative reviews are selected and outlined to illustrate the applications of EXAFS in various physicochemical and biological disciplines. The prime objective of the present review is to describe the various capabilities of EXAFS as a structural tool and to arouse the interested reader to consider, and perhaps to design, his or her structural investigation with this novel tool.

1. INTRODUCTION

EXAFS is an abbreviation for extended X-ray absorption fine structure coined by Lytle [1]. Experimentally it is associated with the oscillatory modulation of the absorption coefficient on the high energy side of and X-ray absorption edge of a given constituent atom in a material. In Fig. 1 an example is given of the EXAFS of nickel metal above its K absorption edge at 8332.8 eV. When an X-ray beam passes through a medium, its intensity is attenuated exponentially according to the classical absorption equation
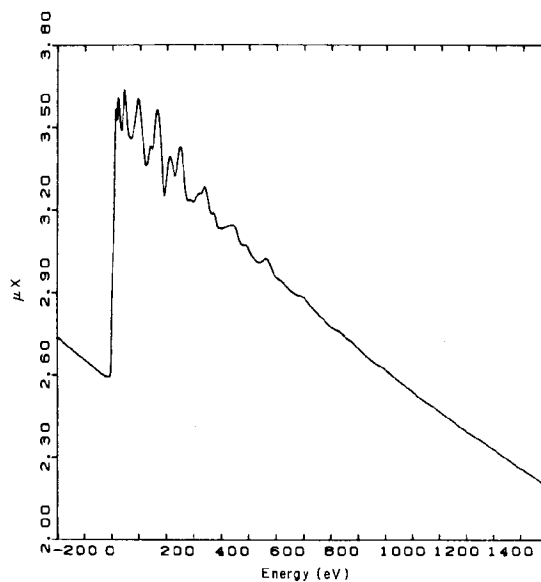
$$I = I_0 \exp(-\mu x) \tag{1}$$

Fig. 1. Experimental EXAFS scan of nickel metal taken with synchrotron radiation above the K absorption edge of nickel at 8332.8 eV. The energy is labeled with reference to the K edge of nickel taken as zero.

where I and I_0 are the transmitted and incident intensities respectively, μ is the linear absorption coefficient and x is the sample thickness. In general, μ is a function of the photon energy. When the X-ray energy $h\nu$ becomes equal to or greater than the binding energy E_b of a core electron, the latter is emitted by a photoelectric process from the atom with a kinetic energy E, conserving energy in the process:

$$E = h\nu - E_b \qquad (2)$$

In pure nickel, when $h\nu = 8332.8$ eV (the binding energy of the innermost K electron in nickel), a sharp increase in μ occurs, giving rise to the characteristic K absorption edge shown in Fig. 1. On the high energy side of the absorption edge, μx exhibits fluctuations with increasing photon energy extending to a few hundred electronvolts beyond the edge. These oscillations are now theoretically understood to be a final state electron effect arising from the interference between the outgoing photoejected electron and that fraction of itself that is backscattered from the neighboring atoms. The interference directly reflects the net phase shift of the backscattered electron in the vicinity of the central excited atom, which is largely proportional to the product of the electron momentum k and the distance traversed by the electron. Both the type of central absorbing atom and the backscattering neighboring atoms (i.e. their positions in the periodic table) also play a significant role in the interference event. As a result, EXAFS has now been realized and proven to be a powerful structural tool for probing the atomic environment of matter, particularly since the advent of intense continuous synchrotron radiation in the X-ray region.

Historically, the fine structure above X-ray absorption edges had been reported as early as 1920 by Fricke [2] and Hertz [3] who worked with the K edges of magnesium-, iron- and chromium-containing compounds and with the L edges of cesium to neodymium. Progress was slow prior to 1970, primarily because the physical processes associated with EXAFS were not well understood (and hence no adequate theory was put forward to account for the observed spectra) and because the experiments were tedious to perform prior to the availability of synchrotron radiation (this point is discussed later).

Various early theories had been proposed to explain the EXAFS and these can be broadly classified into two categories: long-range order and short-range order. The long-range order theories [4, 5] require the existence of lattice periodicity characteristic of crystalline solids and assume transition to quasi-stationary states to explain the fine structure. However, as pointed out by Azaroff [6] and Stern [7], the long-range order theories do not adequately predict the shape of the experimental absorption curve, since the dominant matrix element effects are neglected. The early long-range order theory of Kronig [4] also failed to explain EXAFS in gases and amorphous materials.

However, there is ample experimental evidence supporting the short-range order [7] approach. EXAFS has been observed in simple gaseous molecular systems such as $GeCl_4$ [8] and, more recently, Br_2 [9]. The germanium EXAFS above its K edge in $GeCl_4$ taken with synchrotron radiation [10] is shown in Fig. 2. The fine structure arises from backscattering of the K photoelectron of germanium by the four chlorine atoms bonded to germanium in the tetrahedral molecule. In another early study, Van Nordstrand [11] observed a close similarity in the EXAFS spectra of a series of chromium, manganese and cobalt crystalline compounds to those of their aqueous solu-
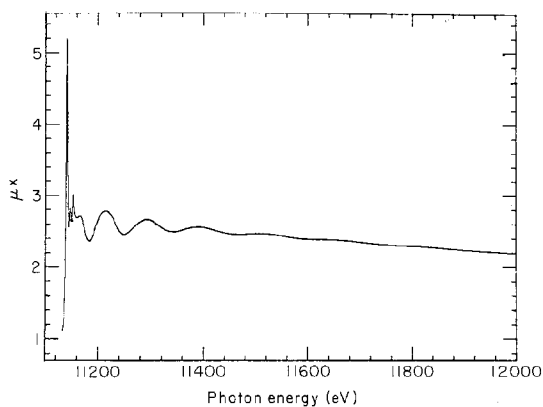

Fig. 2. Experimental EXAFS scan of germanium in a $GeCl_4$ molecule taken with synchrotron radiation above the K absorption edge of germanium at 11 103.3 eV. (After Kincaid [10].) The fine structure arises from backscattering of the K photoelectron of germanium by the chlorine atoms bonded to the germanium atom in the molecule.

tions and concluded that the region of influence in an EXAFS event extended only 4–5 Å from the center of the atom being excited. In solids, perhaps the first convincing experiments to demonstrate the short-range order effects associated with EXAFS were performed by Nelson et al. [12] in 1962. They measured the EXAFS above the K edge of germanium in glassy GeO_2 out to 350 eV and compared it with those of the hexagonal and tetragonal crystalline polymorphs shown in Fig. 3. The EXAFs of glassy and hexagonal GeO_2 (in which germanium is fourfold coordinated by oxygen atoms) were very similar but differed notably from that of tetragonal GeO_2 (in which germanium is sixfold coordinated by oxygen atoms). These observations were later reconfirmed by Lytle [1] in 1965, who extended the measurement to 1100 eV beyond the K absorption edge of germanium. Since no long-range order (i.e. lattice periodicity) exists in the amorphous phase, it is necessary to conclude that the fine structure is most strongly influenced by the arrangement of neighboring atoms about the germanium. A detailed account of the history and modern practice of EXAFS since 1970 has been given by Lytle et al. [13].

In this section the physical mechanism associated with EXAFS in terms of the single-scattering approximation is first discussed. This is followed by instrumentation for
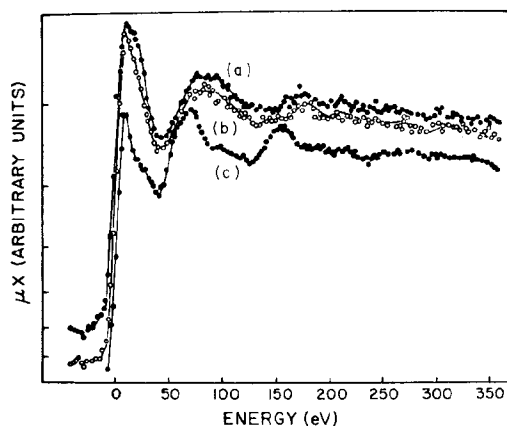

Fig. 3. Experimental K edge EXAFS spectra of GeO_2 (glass) (spectrum (a)), GeO_2 (hexagonal) (spectrum (b)) and GeO_2 (tetragonal) (spectrum (c)) taken by Nelson et al. [12]. The energy is labeled with reference to the K edge of germanium at 11 103 eV taken as zero.

EXAFS experiments, data acquisition using synchrotron radiation as a light source, and data analysis to extract structural information about the central X-ray absorbing atom. The unique features of EXAFS as a structural tool for material characterization will be outlined and further exemplified by a variety of applications in disordered solids such as glasses, catalysts, solutions, biological molecules, defects and impurities in condensed matter. Bonding and chemical information derived from near-edge absorption features within 30 eV of an absorption edge are discussed. Finally, other detection schemes for EXAFS and their applications are also disclosed.

2. FUNDAMENTALS OF EXTENDED X-RAY ABSORPTION FINE STRUCTURE

As noted above, the observation of X-ray absorption fine structure has been known for over half a century. Recent revival of interest in EXAFS began with the work of Sayers et al. [14] in 1970. They showed that using a single-scattering approximation the observed fine structure oscillations may be understood in terms of interference between the outgoing photoelectron wave in the vicinity of the central atom and that portion of it backscattered from neighboring atoms. Furthermore, the problem may be inverted to obtain distances r_j from a Fourier analysis of EXAFS data. In particular, they performed a Fourier transform of EXAFS data in k space for crystalline and amorphous germanium and showed that peaks in the transforms correspond to various atomic shells [15]. It is now recognized that analysis of the EXAFS can yield not only the distance but also the number and type of nearest-neighbor atoms about the central atom.

Another milestone in the development at Stanford University in 1974 [6] of EXAFS was the availability of synchrotron radiation in the X-ray region. The 10^4–10^5 increase in intensity in tunable X-rays over a broad spectral region enables EXAFS spectra with an excellent signal-to-noise ratio to be obtained in a matter of minutes. In the past decade or so, there has been growing appreciation of EXAFS as a new structural tool for studying a wide variety of materials for which conventional techniques such as X-ray diffraction

and conventional electron microscopy are less useful or impossible.

2.1. The physical mechanism

The attenuation of X-rays traversing through a medium occurs by three principal modes: scattering, pair production and photoelectric absorption. In the EXAFS regime, photoelectric absorption dominates the attenuation process, resulting in the total absorption of a photon which in turn gives its full energy to electrons according to eqn. (2). To understand the mechanism that gives rise to the EXAFS oscillations, we consider the K edge fine structure. In the dipole approximation [16] the probability of X-ray absorption is given by

$$p = 2\pi^2 e^2 (\omega c^2 m)^{-1} |M_{fs}|^2 \rho(E_f) \qquad (3)$$

where $M_{fs} = \langle f | \epsilon \cdot p | s \rangle$, $|s\rangle$ is the K shell s state, $\langle f |$ is the final unoccupied state of p symmetry, $\rho(E_f)$ is the density of states per unit energy at the energy E_f of the final state, $2\pi\omega$ is the frequency of the X-ray, p is the momentum operator and ϵ is the electric field vector of the X-ray. For X-ray energies well above the edge, $\rho(E_f)$ gives a monotonic contribu-

tion and can be approximated by that of a free electron of energy $E = \hbar^2 k^2 (2m)^{-1} + E_0$. Here E_0 is the energy of free electrons with $k = 0$ and is the effective mean potential experienced by an excited electron. It is often called the threshold energy. With this assumption for $\rho(E_f)$, the only remaining factor that can contribute to the EXAFS signal is M_{fs}. Now, the initial state $|s\rangle$ is fixed and does not vary with ω. The final state $\langle f |$, however, varies with ω and produces the fine structure.

Further, the wave function of $\langle f |$ is a sum of two contributions. If the atom is isolated, the excited photoelectron would be in a solely outgoing state from the central atom as shown schematically in Fig. 4 by the outgoing solid rings. In this case, M_{fs} exhibits no fine structure and the X-ray absorption coefficient would vary monotonically with ω. This is the case for a monatomic gas such as krypton, the spectrum [10] of which beyond the K edge at 14 326 eV follows a decay predicted by the photoelectric effect and reveals no fine structure (Fig. 5).

If now the X-ray absorbing atom is surrounded by other atoms, as in a molecule such as $GeCl_4$ (Fig. 2) or in the condensed

$$E_2 > E_1$$

$$E_1 \qquad\qquad\qquad E_2$$

(a)   (b)

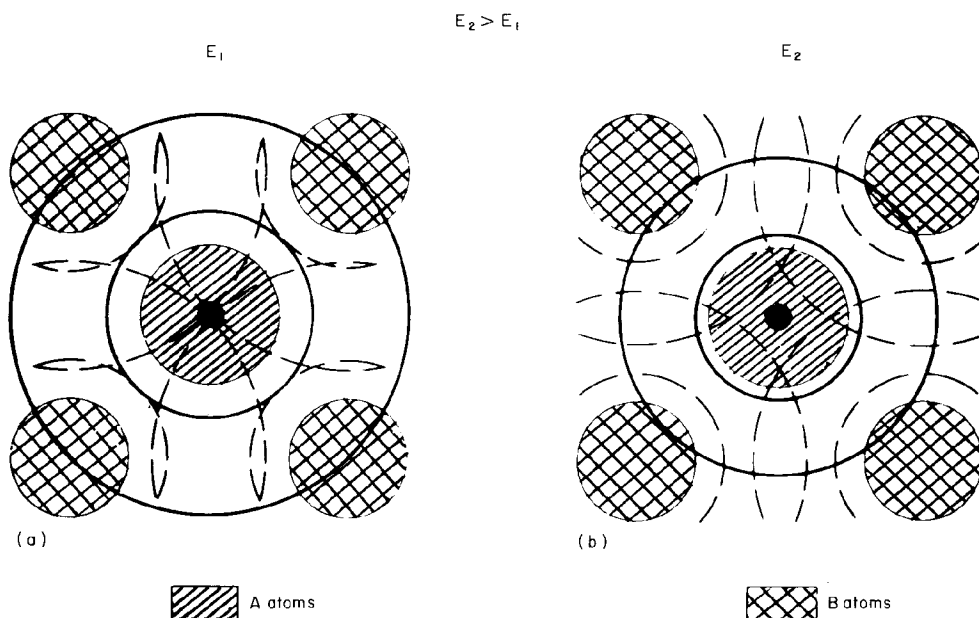▨ A atoms   ⊠ B atoms

Fig. 4. Schematic representation of an EXAFS event. The excited electronic state is centered about the A atom. The full circles represent the crests of the outgoing part of the electronic state. The surrounding B atoms backscatter the outgoing part as shown by the broken circles. Constructive interference is represented in (a) and destructive interference in (b).
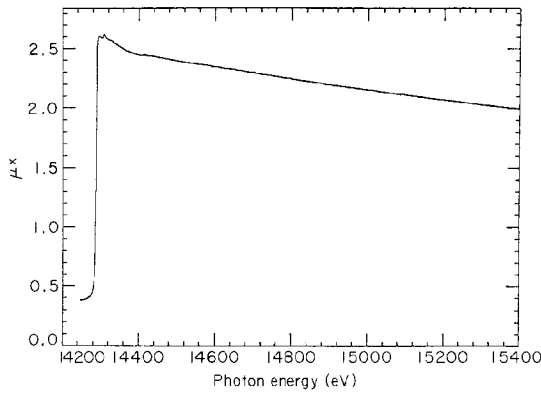
Fig. 5. K edge absorption spectrum of krypton gas. (After Kincaid [10].)

phase, whether liquid, glassy or crystalline, the outgoing electron is scattered by the surrounding atoms to produce incoming waves as depicted by the broken lines in Fig. 4. These incoming or backscattered waves can constructively or destructively interfere with the outgoing wave near the origin where $|s\rangle$ exists. In Fig. 4(a) the amplitudes of the outgoing and backscattered waves add at the central A atom site, leading to a maximum in the X-ray absorption probability. In Fig. 4(b) the X-ray energy has been increased to E_2, leading to a shorter photoelectron wavelength for which the outgoing and backscattered waves interfere destructively at the absorbing A atom site with a resulting minimum in the absorption. This interference gives rise to an oscillatory variation in M_{fs} as ω is varied, changing the electron wavelength and thus the phase between the outgoing and backscattered waves. Constructive interference increases M_{fs} while destructive interference decreases M_{fs} from the isolated atom value.

The total absorption $\mu(k)$ above the absorption edge is then given by

$$\mu(k) = \mu_0(k)\{1 + \chi(k)\} \tag{4}$$

where $\mu_0(k)$ is the smooth varying portion of $\mu(k)$ and physically corresponds to the absorption coefficient of the isolated atom [17]. The fine structure $\chi(k) = \{\mu(k) - \mu_0(k)\}/\mu_0(k)$ is, therefore, due to interference between backscattered and outgoing photoelectron waves in the photoabsorption matrix element.

2.2. The single-scattering approximation

On the basis of the physical ideas discussed in Section 2.1, Sayers *et al.* [14] derived the

first successful working theory of EXAFS. This was subsequently modified by Stern [7] to a more general form and further refined by others [18, 19]. For an unoriented specimen the fine structure above the K or L_I edge can be described by

$$\chi(k) = -\frac{1}{k} \sum_j \frac{N_j}{r_j^2} \exp\left(-\frac{2r_j}{\lambda}\right) \exp(-2\sigma_j^2 k^2) \times$$

$$\times f_j(\pi, k) \sin\{2kr_j + \delta_j(k)\} \tag{5}$$

where $k = \{2m(E - E_0)/\hbar^2\}^{1/2}$ is the wavevector of the ejected photoelectron of energy E and E_0 is the inner potential or threshold energy caused by the atomic potentials and represents the threshold above which the kinetic energy must be added to determine the total energy E. The summation is over shells of atoms which are at a distance r_j from the absorbing atom and contain N_j atoms (the coordination number). λ is the mean free path of the photoelectron. The second exponential containing σ_j^2 is a Debye–Waller type of term where σ_j^2 is not the usual mean square vibrational amplitude of an atom but is the mean square *relative* positional fluctuation of the central and backscattering atoms. The fluctuations may be static (structural disorder) or dynamic (thermal) in origin. In this form the resultant EXAFS is a sum of sine waves with periods $2kr_j$ from each jth shell with an amplitude which represents the number of neighbors modified by an envelope due to the scattering amplitude, the Debye–Waller damping and the mean free path damping. Besides the usual $2kr_j$ which accounts for the phase difference of a free electron making the return trip to the neighbor, additional phase shifts $\delta_j(k)$ are needed to account for the potentials due to both the central atom and the backscatterers. The factor r_j^{-2} arises from the product of the amplitudes of the outgoing and backscattered waves, both of which decay as r_j^{-1} because of their spherical nature. For a single-crystal specimen the factor $3\cos^2\theta_j$ has to be included in the summation, where θ_j is the angle that the jth neighbor makes with the polarization vector of the X-ray. This factor averages to unity for polycrystalline or amorphous materials. Conceptually, EXAFS may be considered to be a mode of electron diffraction where now the source of electrons is generated from within a particular atomic species participating in the absorption event.

The derivation of eqn. (5) is based on the following assumptions.

(i) The atomic radius is small enough for the curvature of the incident wave on the neighboring atoms to be neglected so that the incident wave may be approximated by a plane wave. This is achieved mathematically by replacing the Hankel function by its asymptotic form [19, 20] which in turn yields the factor k^{-1} in eqn. (5).

(ii) Only single scattering by the neighboring atoms is included.

These assumptions have been examined in some detail for f.c.c. copper by Lee and Pendry [19]. They first treated the electron scattering using a spherical wave expansion to take account of the finite size of the atoms. The effects are quite large but appear to make quantitative but not qualitative changes to the single-scattering description. As the size of the scattering atom increases, significant deviations in both the phase and the amplitude are noted between the spherical wave calculation and the asymptotic plane wave approximation [21].

2.3. Multiple-scattering effects

We have seen that the EXAFS phenomenon has been reduced to the problem of the scattering of photoelectrons by atoms analogous to low energy electron diffraction (LEED), in which an electron beam several hundred electronvolts in energy is scattered by a crystal. Since it is well known that multiple scattering is very important in the interpretation of LEED data [22], this immediately raises the question of the adequacy of the single-scattering description for EXAFS. The situation has also been addressed by Lee and Pendry [19] who showed that each multiple-scattering process can be described by an effective interference path length equal to the sum of the scattering paths. In k space they give rise to rapidly oscillating terms which tend to average out. It is only very near the absorption edge within about 30 eV (the so-called X-ray absorption near-edge structure (XANES) [23]) that multiple scattering (band structure and chemical bonding effects) becomes important. This is because at low energy the scattering becomes more isotropic and the electron mean free path becomes very long. Alternatively, if we Fourier transform the data, the multiple-scattering contribution will show up farther out in the transformed spectrum (see Section 2.5). In particular, since the path length for multiple scattering must be larger than that for the dominant first-shell interaction, its contribution will have no influence on the nearest-neighbor distance which is a predominant feature in the radial structure function of disordered systems such as glasses and isolated impurities.

However, multiple scattering in EXAFS is important when an inner shell atom shadows an outer shell atom as was first realized in the fourth shell in the copper EXAFS which has an anomalously large amplitude and phase shift. The reason for this observation is that in an f.c.c. lattice a nearest-neighbor atom is directly in the line of sight of the fourth-shell atom. The outgoing electron is strongly forward scattered, thereby enhancing the electron amplitude in the fourth shell [19]. This gives rises to the so-called "focusing" effect analogous to amplifying a relay system. This focusing effect has been used to advantage by Teo [24] who developed a formalism to determine the bond angle of nearly collinear systems such as those of M—C—O in metal-carbonyl complexes.

3. SYNCHROTRON RADIATION AS A LIGHT SOURCE FOR EXTENDED X-RAY ABSORPTION FINE STRUCTURE EXPERIMENTS

The two sources of continuous X-radiation used for EXAFS experiments are the bremsstrahlung output from a rotating anode X-ray tube and the synchrotron radiation produced from electron storage rings or synchrotrons. We have seen that EXAFS deals with the fine attenuation, 5%–10% in relative magnitude, on the high energy side of a steeply rising absorption edge. To ensure that we are measuring an EXAFS signal, good signal-counting statistics must be obtained to yield a high signal-to-noise ratio (greater than 300 to 1). To achieve this with a conventional X-ray tube and a flat dispersing crystal, an experimental scan such as one of those shown in Fig. 3 for the GeO_2 polymorphs typically takes a week or more. The procedure is tedious and time consuming. Source instability over such an extended period of operation adds to the problem. With the advent of synchrotron radiation sources in the X-ray region, particularly

that at the Stanford Synchrotron Radiation Laboratory [25, 26], a second important milestone was reached in the development of modern EXAFS.

Synchrotron radiation is emitted as the major loss mechanism from charged particles such as electrons and positrons in a circular motion at relativistic energies. The properties of synchrotron light emitted from electrons with velocities near that of the light are drastically different from the classical dipole radiation [27] and demonstrate the importance of synchrotron radiation as a new and powerful light source [28]. The properties have been measured by Elder et al. [29] and studied theoretically by Schwinger [27] and may be summarized [25, 26] as follows: (i) continous spectral distribution from the IR to the X-ray region which is ideal as a light source for UV and X-ray spectroscopies; (ii) higher intensity, permitting the use of monochromators with a narrow band pass; (iii) plane polarization, with the electric vector in the orbital plane of the circulating particles; (iv) extremely high collimation which is important to the lithography of submicron structures; (v) sharply pulsed time structure. Synchrotron radiation was experimentally discovered using the General Electric 70 MeV betatron in 1947 [29]. A detailed historical account of the discovery of synchrotron radiation has recently been revealed by Pollock [30].

The spectral distribution of synchrotron radiation from the Stanford Position Electron Accelerator Ring (SPEAR) [26] is shown in Fig. 6 with the electron beam energy E_e from 1.5 to 4.5 GeV as the parameter. As can be seen, it is an intense continuous distribution extending from the IR and into the X-ray region. With this spectral distribution and the transmission characteristic of the beryllium window assembly, useful X-ray fluxes in the range from 3.5 keV to approximately 30 keV for a 3.5 GeV electron beam are available in SPEAR. This permits the K edge EXAFS of potassium (K edge energy, 3.60 keV) to cadium (K edge, 26.71 keV) and the L edge EXAFS of indium (L_3 edge, 3.70 keV) to uranium (L_3 edge, 17.17 keV) to be measured routinely.

Compared with the bremsstrahlung output of a 12 kW standard X-ray tube, synchrotron radiation is higher in intensity by a factor of about 10^6. This reduces the measurement time
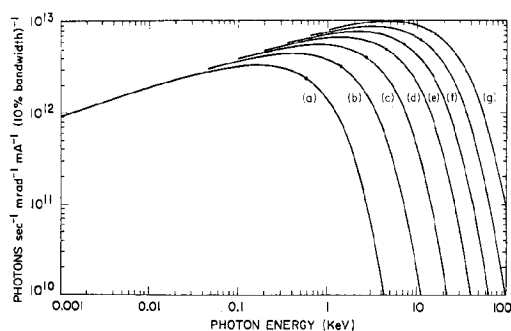

Fig. 6. Spectral distribution of synchrotron radiation from SPEAR having a radius of curvature of 12.7 m. (After Doniach et al. [26].)

Curve	ϵ_c (keV)	E_e (GeV)
(a)	0.58	1.5
(b)	1.4	2.0
(c)	2.7	2.5
(d)	4.7	3.0
(e)	7.4	3.5
(f)	11	4.0
(g)	15.7	4.5

for a typical EXAFS experiment from a week or more to an hour or less. In Fig. 7, we compare the K edge EXAFS spectrum of arsenic in glassy As_2Te_3 taken by Pettifer [31] with that of a conventional X-ray tube and synchrotron radiation. The spectrum shown in Fig. 7(a) is the summation of seven individual scans, each of which took 3 days of continuous scanning. The synchrotron spectrum shown in Fig. 7(b) was taken in 1.3 h. The product of the increase in resolution multiplied by the measurement time multiplied by the signal-to-noise ratio of the two spectra shows an improvement of about 3×10^4 of the synchrotron data over that obtained using a conventional source [31].

In Fig. 8(a) the apparatus used for transmission EXAFS measurements at Stanford Synchrotron Radiation Laboratory is shown schematically [32]. The X-ray beam from the SPEAR vacuum chamber passes successively through a helium chamber, a beryllium window, a slit, a channel-cut crystal monochromator, a mask, ion chamber 1 which measures I_0, a sample and ion chamber 2 which measures I. The experiment is controlled by a PDP-11/34 minicomputer with interfaces to control the angle of the crystal monochromator, to digitize the ion chamber currents
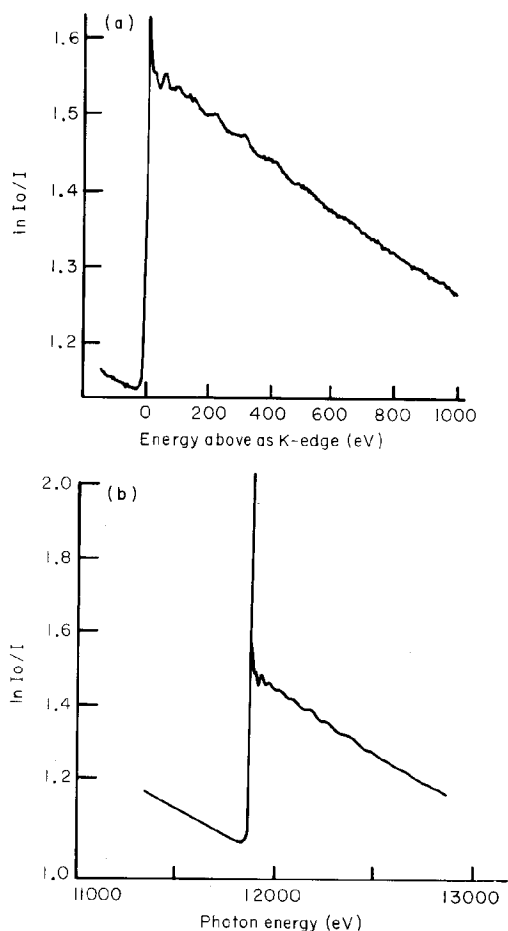
Fig. 7. K edge EXAFS spectra of arsenic in As_2Te_3 glass taken with (a) a conventional X-ray tube and (b) synchrotron radiation. The spectrum in (a) is a summation of seven scans, each of which took 3 days of continuous scanning. The spectrum in (b) was taken in 1.3 h. The sharp white line in the synchrotron radiation spectrum is due to higher resolution (about 2 eV) compared with about 8 eV for the data taken with the X-ray tube. (After Pettifer [31].)

Fig. 8. Schematic diagram of the EXAFS experimental apparatus at Stanford Synchrotron Radiation Laboratory: (a) transmission mode and (b) fluorescence mode of detection.

and to store and plot the ratio I_0/I. For dilute systems a fluorescence technique [33] has been devised to enhance experimentally the relatively weak EXAFS signal from the bulk absorption background of the host matrix. This detection scheme utilizes the fact that an inner shell vacancy may relax by undergoing a radiative transition from a higher energy occupied shell. The fluorescence yield is a monotonically increasing function of atomic number and is expected to be independent of excitation energy above the threshold but may vary slightly near the threshold. Thus the

fluorescence intensity is a direct measure of the absorption probability, which is the mechanism of interest in EXAFS. In Fig. 8(b) a typical fluorescence EXAFS set-up is shown schematically. The original scheme [33] has been further modified for improved solid angle collection, filtering of Compton and elastic scattering of the incident beam by the specimen [34] and discriminative energy detection [35, 36].

Further experimental details associated with EXAFS measurements have been given by Lytle et al. [37] and in a number of authoritative review articles [38-43]. Since its opening in 1974, the request for beam time for X-ray experiments at Stanford Synchrotron Radiation Laboratory has been doubled every year, as judged from the number of work proposals submitted to Stanford for beam time. This has led to a recently revived interest [44] in in-house laboratory EXAFS apparatus constructed using more powerful rotating anode sources for X-ray generation in conjunction with curved-crystal optics [45-48]. Also, as a consequence of the demand of the scientific community, various synchrotrons all over the world are now being up-

TABLE 1

Synchrotron radiation sources

Machine	Location	Energy (GeV)	Current (mA)	Bending radius (m)	Critical energy (KeV)	Remarks
PETRA	Hamburg, Germany	15	50	192	39.0	Possible future use for synchrotron radiation research
PEP	Stanford, CA, U.S.A.	15	50	165.5	45.2	Synchrotron radiation facility planned
		12	45	(23.6)	(163)	(From 17 kG wiggler)
CESR (Cornell)	Ithaca, NY, U.S.A.	8	50	32.5	35.0	Used parasitically
VEPP-4	Novosibirsk, U.S.S.R.	7	10	16.5	46.1	Initial operation at 4.5 GeV
		4.5		(18.6)	(10.9)	(From 8 kG wiggler)
DORIS	Hamburg, F.R.G.	5	50	12.1	22.9	Partly dedicated
		2.5	300		2.9	
SPEAR	Stanford, CA, U.S.A.	4.0	50	12.7	11.1	50% dedicated
		3.0	100		4.7	
		3.0		(5.5)	(10.8)	(From 18 kG wiggler)
SRS	Daresbury, Gt. Britain	2.0	500	5.55	3.2	Dedicated
				(1.33)	(13.3)	(For 50 kG wiggler)
VEPP-3	Novosibirsk, U.S.S.R.	2.25	100	6.15	4.2	Partly dedicated
				(2.14)	(11.8)	(From 35 kG wiggler)
DCI	Orsay, France	1.8	500	4.0	3.63	Partly dedicated
ADONE	Frascati, Italy	1.5	60	5.0	1.5	Partly dedicated
				(2.8)	(2.7)	(From 18 kG wiggler)
VEPP-2M	Novosibirsk, U.S.S.R.	0.67	100	1.22	0.54	Partly dedicated
ACO	Orsay, France	0.54	100	1.1	0.32	Dedicated
SOR Ring	Tokyo, Japan	0.40	250	1.1	0.13	Dedicated
SURF II	Washington, DC, U.S.A.	0.25	25	0.84	0.041	Dedicated
TANTALUS I	Stoughton, WI, U.S.A.	0.24	200	0.64	0.048	Dedicated
PTB	Braunschweig, F.R.G.	0.14	150	0.46	0.013	Dedicated
N-100	Kharkov, U.S.S.R.	0.10	25	0.50	0.004	
Photon factory	Tsukuba, Japan	2.5	500	8.33	4.16	Dedicated
				(1.67)	(20.5)	(For 50 kG wiggler)
NSLS	Brookhaven National Laboratory, NY, U.S.A.	2.5	500	6.88	5.01	Dedicated
				(1.67)	(20.5)	(For 50 kG wiggler)
BESSY	West Berlin, F.R.G.	0.80	500	1.83	0.62	Dedicated; industrial use planned
NSLS	Brookhaven National Laboratory, NY, U.S.A.	0.70	500	1.90	0.40	Dedicated
ETL	Electrotechnical Laboratory, Tsukuba, Japan	0.66	100	2	0.32	Dedicated
UVSOR	Institute of Molecular Science, Okatabi, Japan	0.60	500	2.2	0.22	Dedicated
MAX	Lund, Sweden	0.50	100	1.2	0.23	Dedicated
KURCHATOV	Moscow, U.S.S.R.	0.45		1.0	0.21	Dedicated

dated and new facilities built as a dedicated source for synchrotron radiation research [49] (Table 1).

4. DATA ANALYSIS

4.1. General consideration

Experimentally the EXAFS spectrum shown in Fig. 1 appears as low intensity oscillations (relative to the jump at the absorption edge) superimposing on the smooth atomic absorption background which decays with increasing energy above the absorption edge. The fine structure according to eqn. (4) is therefore given by $\chi(k) = \{\mu(k) - \mu_0(k)\}/\mu_0(k)$ where $\mu(k)$ is the total absorption measured above the edge and $\mu_0(k)$ is the smooth atomic contribution. To extract the EXAFS signal $\chi(k)$ from the experimental X-ray absorption spectrum, a fairly standardized procedure has been established [37, 40, 50, 51]. This consists of correcting for spectrometer shift, deglitching, pre-edge and post-edge background removal, edge normalization, extraction of the EXAFS signal $\chi(k)$, Fourier transform of $\chi(k)$ and inverse transform to isolate the EXAFS contribution from a selected region in real space.

4.2. Background removal

Since the smooth absorption $\mu_0(k)$ of an isolated atom is not generally available experimentally and since present theoretical calculations of $\mu_0(k)$ are not sufficiently accurate for most EXAFS work (about 0.1%), it is assumed that the smooth part of $\mu(k)$ represents the desired $\mu_0(k)$. With this assumption, the remaining oscillatory part of $\mu(k)$ is taken as $\Delta\mu = \mu(k) - \mu_0(k)$ to yield $\chi(k) = \Delta\mu(k)/\mu_0(k)$. The post-edge background above 30 eV in the EXAFS region may then be generated analytically by fitting $\mu(k)$ (including the EXAFS) to a series of cubic splines [52] of equal segments. The ends of each segment are so connected that the derivatives are continuous across the ends. Three to five such splines are found adequate for data extending 1000 eV above the absorption edge. When the number of segments is too small, the background is not separated well enough; when the number is too large, the background follows the EXAFS oscillations, especially at low energies, and "robs" its intensity [51]. A least-squares

fit with such a spline function readily enables the removal of low frequency background components from $\mu(k)$ without affecting the higher frequency EXAFS oscillations. It is noted that spline fitting is essentially a local fitting procedure in that the polynomial function within each interval is mainly determined by the local quality of the fit. The pre-edge background in the range from -200 to -20 eV is obtained simply by a linear regression analysis of the first ten raw data points.

The result is shown graphically in Fig. 9 for nickel. The full line in Fig. 9(a) is the raw experimental K edge EXAFS scan of a nickel foil 5 μm thick taken at 90 K. The spectrum was recorded at Stanford Synchrotron Radiation Laboratory with SPEAR running at an electron energy of 2.6 GeV and a beam current of about 30 mA. The broken line in Fig. 9(a) is the smooth post-edge background derived from a cubic spline fitting with five segments in the range 30–1200 eV.

Other background removal methods such as a single polynomial fit over the whole range of the data, the sliding box-car window fitting [41] and others have been tried. All these procedures suffer, however, in that a single poor data point or noise or end point effects can introduce systematic errors.

4.3. Extraction of extended X-ray absorption fine structure

The energy scale is converted to the k scale using $k = \{0.263(E - E_0)\}^{1/2}$ where E_0 is the energy threshold of the absorption edge and is experimentally located by the first maximum in the derivative spectrum of the absorption curve. The EXAFS $\chi(k)$ at energies above about 30 eV is now obtained by subtracting the smooth post-edge background $\mu_0(k)$ from the measured absorption $\mu(k)$ and dividing by the step jump S at the absorption edge using the correction $M(k)$ of McMaster et al. [17] as a function of energy:

$$\chi(k) = \frac{\mu(k) - \mu_0(k)}{SM(k)} \tag{6}$$

This procedure yields the normalized $\chi(k)$ which is then weighted by k to yield the familiar χk versus k plot given in Fig. 9(b). The k weighting or more generally the k^n weighting will be discussed below in conjunction with Fourier analysis.
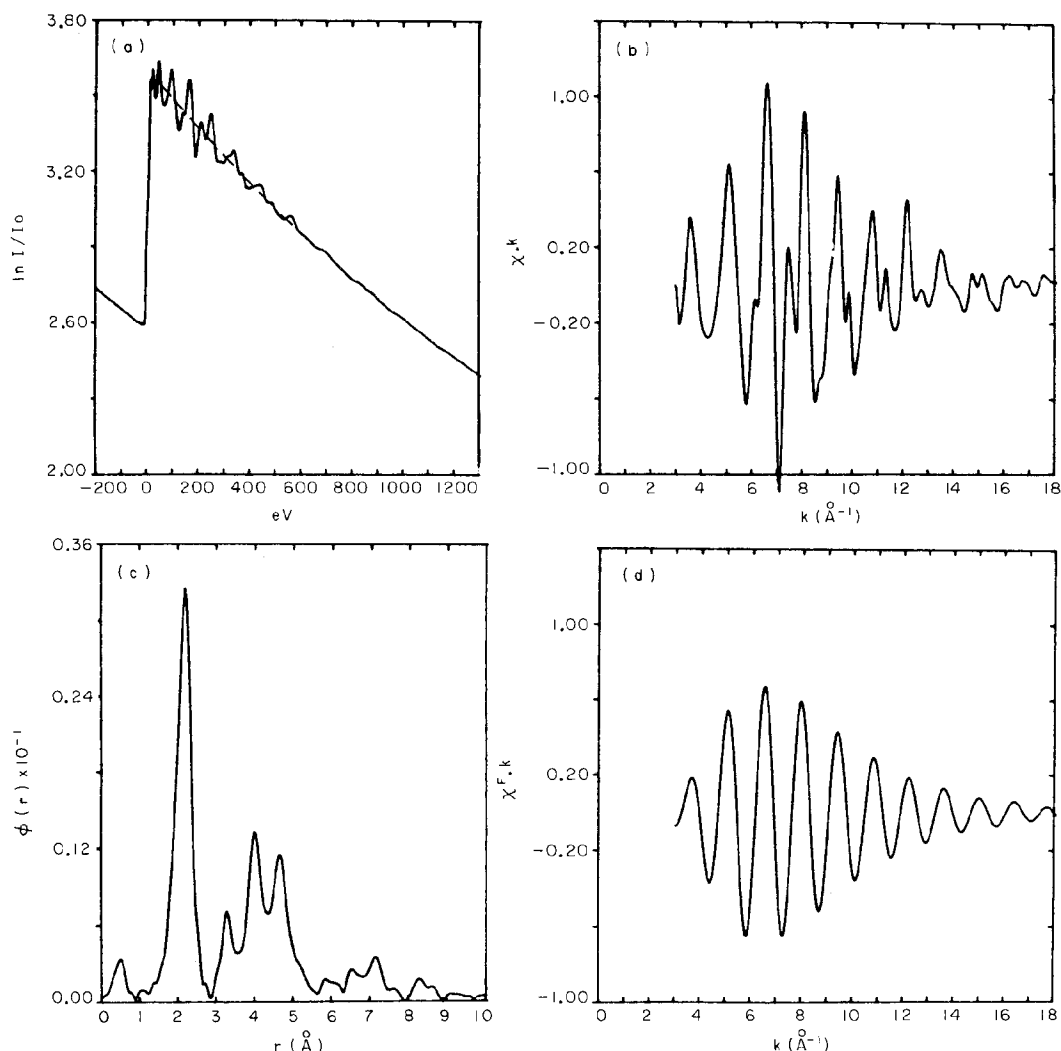
Fig. 9. Graphical representation of a typical EXAFS data analysis: (a) experimental scan of the K edge EXAFS of nickel in pure nickel at 90 K (- - -, a spline fit of the smooth post-edge background absorption above the absorption edge); (b) normalized EXAFS plotted as χk vs. k with a Hanning window applied to the first and last 5% of the k space data; (c) Fourier transform of (b) according to eqn. (8); (d) inverse transform of the first shell in (c) in the region 1–2.8 Å.

4.4. Fourier transform to r space

If we return to eqn. (5), the expression for $\chi(k)$ can be Fourier transformed to yield a radial structure function $\phi(r)$ which contains structural information about the absorbing atom. The Fourier inversion [15] represents a significant step in the development of modern EXAFS and converts it from a qualitative effect to a quantitative effect [37]:

As seen from eqn. (7), the Fourier transform $\phi(r)$ of the EXAFS consists of a sum of radial peaks located at r_j and determines the spatial variation of the scattering matrix. Since in actual practice an EXAFS spectrum is taken over a finite energy range (and hence k space), the Fourier transform that is actually taken is

$$\phi(r) = (2\pi)^{-1/2} \int \chi(k) \, \exp(2ik) \, dk = \sum_j N_j \int \frac{dr'}{r^2 T(r-r')} \exp\left\{-\frac{2(r-r'_j)^2}{\sigma_j{}^2}\right\} \tag{7}$$

$$\phi(r) = (2\pi)^{-1/2} \int\limits_{k_{\min}}^{k_{\max}} W(k)k^n\chi(k) \exp(2ikr) \, dk$$

(8)

where $k_{\max}$ and $k_{\min}$ are the maximum and minimum k values of the usable experimental data. k^n is a weighting function used to compensate for amplitude reduction as a function of k [37], especially for low Z scatterers. n values of 1, 2 and 3 have been suggested by Teo and Lee [52] for backscatterers with $Z >$ 57, $36 < Z < 57$ and $Z < 36$ respectively. Also, as noted by Stern et al. [50], the χk transform is rather sensitive to $k_{\min}$ in the region between the origin and r_1, the first peak in $\phi(r)$. The χk^3 transform may be approximated to a pseudo-charge density which is rather insensitive to $k_{\min}$ and E_0. The k^3 transform weights less at low k and more at high k, where the EXAFS effect is better approximated by the single-scattering expression given in eqn. (5) but is experimentally of poorer quality because of a poorer signal-to-noise ratio.

The factor $W(k)$ on the right-hand side of eqn. (8) is a window function which, when multiplied by the integrand, converts our finite data set to an infinite set that is necessary for Fourier transform. This is done by choosing functions which smoothly set the raw data points to zero at $k_{\min}$ and $k_{\max}$. An example of $W(k)$ is a Hanning function [53] defined in terms of k as follows:

$$W(k) = \frac{1}{2}\left\{1 - \cos 2\pi\left(\frac{k - k_{\min}}{k_{\max} - k_{\min}}\right)\right\}$$

(9)

It is easily seen that $W(k) = 0$ at $k = k_{\min}$ and $k = k_{\max}$. This window function is applied to the first and last 5% of the normalized nickel data discussed above and plotted as χk versus k in Fig. 9(b). The Fourier transform so obtained is shown in Fig. 9(c). Here we note that the transform is made with respect to $\exp(2ikr)$ without including the phase shift $\delta_j(k)$. This has the effect of shifting all the peaks in $\phi(r)$ closer to the origin to $r_j - \delta'$ where δ' is some average of the first derivative of $\delta_j(k)$ with respect to k. In Fig. 9(c) the first peak is the nearest-neighbor position in f.c.c. nickel shifted to 2.24 Å. The crystallographic value from diffraction is 2.492 Å, so that δ' for $j = 1$ is 0.25 Å.

In general the effect of $\delta_j(k)$ on the transform may empirically be corrected for by measuring the EXAFS spectrum of a standard or model compound of known structure. Indeed, as in complex biomolecules, a number of such model compounds are used on a trial-and-error basis to deduce a model of the unknown structure. Alternatively, theoretical values of $\delta_j(k)$ such as those of Teo and Lee [52] can be used in the Fourier transform and r_j can be obtained directly.

Figure 9(d) is an inverse transform of the first shell in Fig. 9(c) in the region 1–2.8 Å. This essentially isolates the EXAFS contribution due to the 12 nearest neighbors. The inverse signal in k space can then be used to derive structural parameters by the simulation to be discussed in Section 4.5.

To illustrate the use of EXAFS as a phase identification tool (like powder X-ray diffractometry), an example is given here for the characterization of metal impurities incorporated in synthetic diamond crystals [54] during growth at a high temperature and a high pressure. In Fig. 10(a) the room temperature K edge EXAFS of nickel from the nickel impurity in synthetic diamond is plotted as χk versus k. The corresponding Fourier transform is shown on the right-hand side and is plotted as $\Phi(r)$ versus r where r is the radial distance from the central atom. The corresponding results for nickel metal and Ni_3B are shown in Fig. 10(b) and Fig. 10(c) respectively. The spectrum of nickel in the synthetic diamond is directly identifiable with that of pure nickel, which yields a radial structure function (right-hand side of Fig. 10(b)) which is characteristic of the f.c.c. structure and consists of four resolved peaks associated with the first four coordination shells about the central atom (cf. Fig. 9 for nickel at 90 K). Ni_3B, like Ni_3C, has a cementite structure: V_h^{16} (Pbnm) and $Z = 4$ [55]. There are two non-equivalent nickel sites: Ni(I) has 11 nickel neighbors at distances ranging from 2.43 to 2.74 Å, two boron atoms at about 2.0 Å and one boron atom at 2.30 Å; Ni(II) has 12 nickel atoms at distances ranging from 2.50 to 2.79 Å, two boron atoms at 2.05 Å and one boron atom at 2.60 Å. The nickel EXAFS in Ni_3B shown in Fig. 10(c) is quite different from that found in the synthetic diamond. The Fourier transform shown on the right-hand side of Fig. 10(c) consists basically of a radial
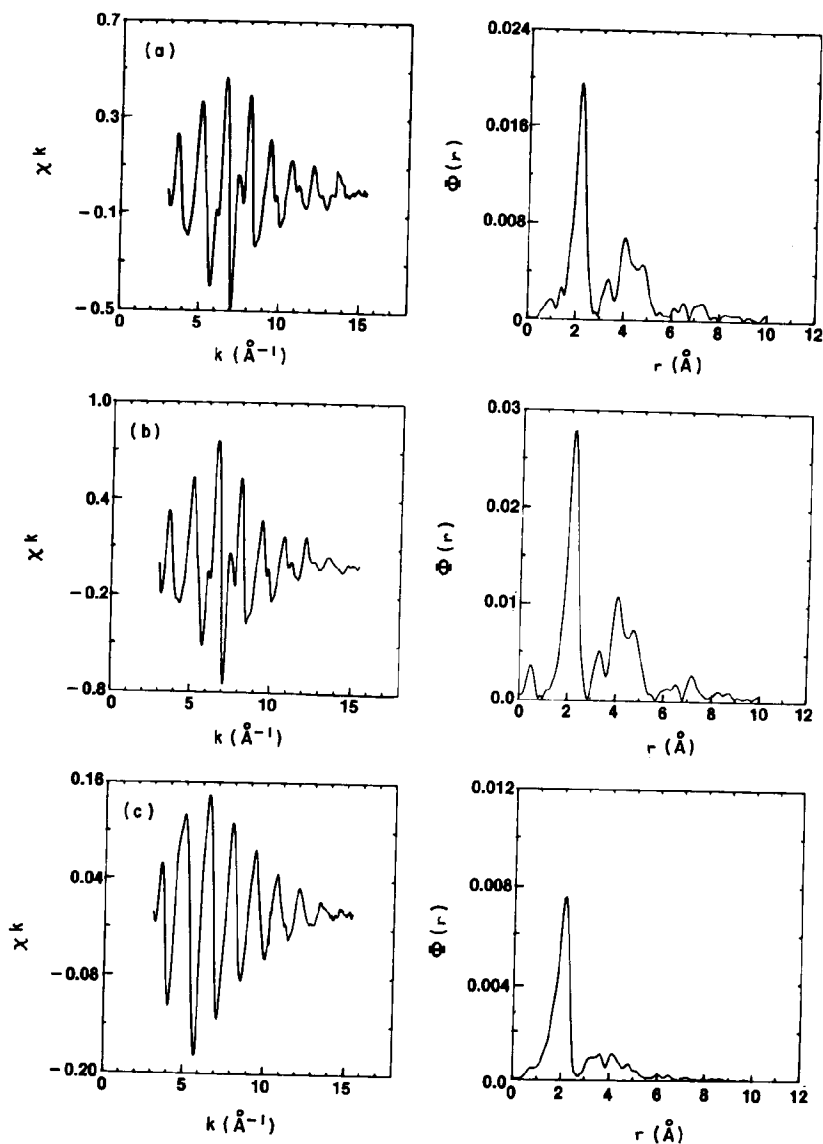
Fig. 10. Normalized K edge EXAFS of nickel plotted as χk vs. k and the corresponding Fourier transform for (a) nickel impurity in synthetic diamond, (b) f.c.c. nickel metal and (c) Ni_3B. R is the radial distance (phase shift not included) from a central X-ray absorbing nickel atom.

peak centered at about 2 Å, which is rather broad, reflecting the distribution of Ni–Ni distances in the structure. No dominant features are evident beyond 3 Å in the radial structure function. Thus, EXAFS can be used to "fingerprint" an unknown phase containing a selectively known constituent element.

4.5. Structural information in k space

Besides interatomic distances r_j, EXAFS contains other structural information such as the coordination number N_j, the type of jth atom in the shell at r_j and their relative mean square disorder σ_j^2 about the average distance r_j. These structural parameters may be obtained by measuring the EXAFS of model compounds under identical conditions and using "transferability" of phase shifts [56]. The structure of the unknown is then modeled by curve-fitting procedures so as to arrive at a calculated EXAFS that best fits the experimental values. A useful way to perform mod-

eling is in combination with back Fourier transformation, especially in systems where the coordination shells are well separated in r space or whose $\phi(r)$ is dominated by the nearest-neighbor shell as in amorphous materials. The shell-by-shell back Fourier transform enables a self-consistent phase shift and experimental envelope function to be determined for each jth shell. Various curve-fitting routines for extracting structural information from EXAFS data have been prescribed [20, 42, 50, 57–59]. A more widely used procedure [59] is described below.

If we recall the single-scattering expression given in eqn. (5), the observed EXAFS $\chi(k)$ may be described by

$$\chi(k) = -\frac{1}{k} \sum_j A_j \sin\{2r_j k + \delta_j(k)\} \qquad (10)$$

having oscillatory terms with frequencies $2r_j k + \phi_j(k)$ and amplitude terms A_j given by

$$A_j = \frac{N_j}{r_j^2} f_j(\pi, k) \exp\left(-\frac{2r_j}{\lambda}\right) \exp(-2\sigma_j^2 k^2) \quad (11)$$

The parameters on the right-hand side of eqns. (10) and (11) may be classified as (a) scattering parameters (the phase shift $\delta_j(k)$, the backscattering amplitude $f_j(\pi, k)$ and the mean free path λ) and (b) structural parameters (the coordination number N_j, the bond distance r_j and the Debye–Waller factor σ_j). The summation is over all coordination shells j participating in the EXAFS event. In a model system for which N_j and r_j are known crystallographically, EXAFS may be used to generate a set of self-consistent scattering parameters; this information can then be applied to an unknown system of similar chemical nature (e.g. a glass of the same composition) to determine structural parameters.

A least-squares procedure [59] is set up to minimize the variance S where

$$S = \sum_i^n (\chi_i^F - \chi_i)^2 \qquad (12)$$

Here χ_i^F are the Fourier-filtered experimental data and χ_i is the analytical expression given in eqn. (10) which describes χ_i^F for n data points. Since $\chi(k)$ is not a linear function of the various parameters, a Taylor series expansion is used which expresses $\chi(k)$ in terms of approximate parameter values P_j and param-

eter adjustments $\Delta P_j = P_j - P_j'$. When the least-squares condition is applied, a set of simultaneous equations is obtained in terms of ΔP_j rather than P_j. The equations are solved for the adjustment ΔP_j, and the parameters were adjusted by ΔP_j to give a new set of estimates. The procedure was then reiterated with the new estimates P_j' and so on until the new solution differed from the last by less than a desired value, which is usually 1%.

Outlined below is an example of generating the phase and envelope function for the Ni–Ni pair [60]. This is achieved by performing a self-fitting of the filtered EXAFS (Fig. 9(d)) of the first shell of 12 nearest neighbors in f.c.c. nickel metal with the following fixed inputs: $N_1 = 12$, $r_1 = 2.492$ Å, $\Delta E_0 = 0$ and $\sigma_1^2 = 0$. The fitting was performed in χk^3 space to weigh the contribution of nickel at high k. The results are shown in Fig. 11, where the full curve denotes the filtered experimental EXAFS and the crosses denote the simulated spectrum. This simulation has a standard deviation of 5% of the maximum amplitude of the experimental $\chi^F k^3$ spectrum. The Ni–Ni phase parameters so obtained can then be used as initial inputs to simulate the filtered transform arising from the Ni–Ni subshells in crystalline Ni_2B. In turn, the Ni–Ni phase shifts as derived from crystalline Ni_2B have
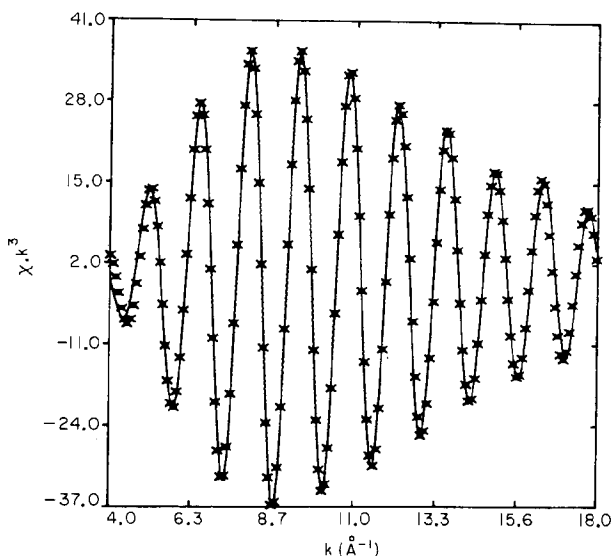
Fig. 11. Experimental (——) and simulated (X) EXAFS of the first shell of 12 neighbors in the region 1–2.8 Å about a nickel atom in f.c.c. nickel metal at 90 K.

been transferred directly to determine Ni–Ni bond distances and coordination numbers of the various subshells in amorphous Ni_2B. Details of such systematic simulations have been described in a number of studies [60–62].

5. NEAR-EDGE STRUCTURE

In EXAFS analysis for structural determination, the data within about 30 eV of the edge are generally ignored because their interpretation is complicated by multiple-scattering and chemical bonding effects. Phenomenologically, as the region near an X-ray absorption edge is scanned in energy, the ejected photoelectron sequentially probes the empty electronic levels of the material. The resulting XANES [23] spectrum within 30 eV of the threshold has now been realized to be rich in chemical information and is receiving increasing attention. While the study of XANES in general has a long history [63], with the availability of intense and well-collimated synchrotron X-radiation sources and the improved experimentation discussed in Section 2.4, these spectra can now be measured more quickly simply, and with greater resolution than ever before.

Vanadium forms a series of oxides over a range of formal oxidation states. The crystal structures of VO, V_2O_3, V_4O_7, V_2O_4 and V_2O_5 are known. These oxides provide a useful series of materials for systematic study of the effects of valence site symmetry and coordination geometry on the XANES spectrum of the central metal atom coordinated by the same ligand [64]. VO has an NaCl structure with regular octahedral VO_6 units. V_2O_3 has a corundum structure in which V^{3+} ions are sixfold coordinated by oxygen ions at two distinct distances of 1.96 and 2.06 Å. V_4O_7 is a mixed valence oxide consisting of both V^{3+} and V^{4+} ions. The structure consists of a distorted h.c.p. oxygen array with vanadium atoms occupying the octahedral sites (distorted) so as to form rutile blocks which extend indefinitely in the triclinic a–b plane. The rutile blocks are four octahedra thick along the perpendicular to this plane. There are four crystallographic non-equivalent vanadium sites with V–O distances ranging from 1.883 to 2.101 Å. The crystal structure of V_2O_4 is monoclinic and is a distorted form of rutile.

The vanadium atoms are again sixfold coordinated by oxygen atoms but are much displaced from the center of the octahedron, resulting in a short V—O bond of 1.76 Å. In V_2O_5 the vanadium atom is fivefold coordinated in a distorted tetragonal pyramid of oxygen atoms. The apex oxygen distance is only 1.585 Å whereas the basal V–O distances vary from 1.78 to 2.02 Å. The site symmetry of the vanadium atom decreases from O_h in VO to C_3 in V_2O_3, to C_1 in both V_4O_7 and V_2O_4, and to C_s in V_2O_5.

In Fig. 12 the K edge XANES spectra of vanadium in these oxides exhibit a pre-edge absorption feature which grows in intensity on going from V_2O_3 to V_2O_5, followed by a weak shoulder on a rising absorption curve (the absorption edge) which culminates in a strong peak in the vicinity of about 20 eV. This strong peak has been assigned as the allowed transition 1s → 4p [65], the lower energy shoulder as the 1s → 4p shake-down transition and the pre-edge feature at threshold as the forbidden transition 1s → 3d [65]. At energies equal to and above the 1s → 4p transition, absorption features may arise from transition to higher np states, shape resonances [66] and/or multiple scattering [67]. The latter two effects are much more complicated to analyze.

Since the initial 1s state is a gerade state, the 1s → 3d transition is strictly dipole forbidden as it is in VO which contains regular octahedral VO_6 units having a center of inversion. When the symmetry of the ligands is lowered from O_h, the inversion center is broken as in V_2O_3, V_4O_7 and V_2O_4 with distorted octahedral VO_6 groups, and in V_2O_5 with distorted square pyramidal VO_5 groups. The pre-edge absorption becomes dipole allowed as a result of a combination of stronger 3d–4p mixing and overlap of the metal 3d orbitals with the 2p orbitals of the ligand [65].

The intensity variation of the pre-edge peak across the oxide series is noteworthy. As seen in Fig. 12, the oscillator strength increases with progressive relaxation from perfect octahedral symmetry (as in VO) to distorted octahedral VO_6 groups (as in V_2O_3, V_4O_7 and V_2O_4) and to a lower coordination with a short V—O bond in a square pyramidal symmetry (as in V_2O_5). The "molecular cage" effect on the oscillator strength of this transition to the 3d orbitals in K edge spectra as
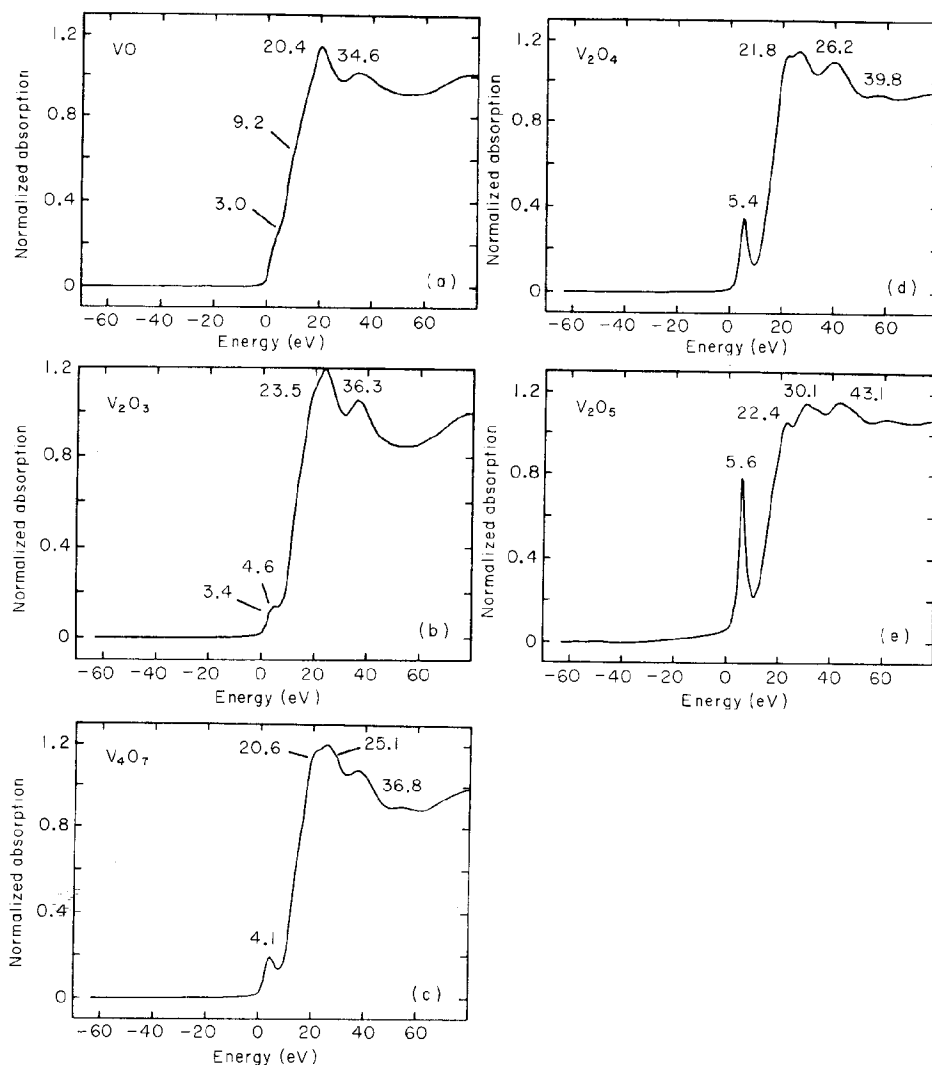
Fig. 12. The K edge XANES spectra of vanadium in a series of vanadium oxides: (a) VO; (b) V_2O_3; (c) V_4O_7; (d) V_4O_8; (e) V_2O_5. The zero of energy is taken at the K edge of vanadium metal at 5465 eV in all cases.

noted by Kutzler et al. [68] appears to be operative here.

Closer examination of the spectrum of V_2O_3 shows that there is a multiplet structure in the pre-edge peak region. The multiplet structure shows splitting of about 1.3 eV and about 2.0 eV. The splittings in the 1s → 3d transition are caused by crystal field splitting of the ground state [65], and in V_2O_3 the d levels of V^{3+} ions in the site with C_3 symmetry are split into A plus 2E states.

The energy positions of various absorption features are found to be correlated with the oxidation state (formal valency) of vanadium in the oxides. With increase in oxidation state, (a) the absorption threshold as defined by the position of the first peak in the derivative spectrum, (b) the absorption edge as defined by the second peak in the derivative curve, (c) the energy of the pre-edge peak and (d) the 1s → 4p transition above the absorption edge all shift to higher energies. The energy shifts, the so-called chemical shifts, are found to follow Kunzl's law [69] and vary linearly with the valence of the absorbing vanadium atom as shown in Fig. 13. The positive shift in the threshold energy with valence increase can be understood conceptually to be due to an in-
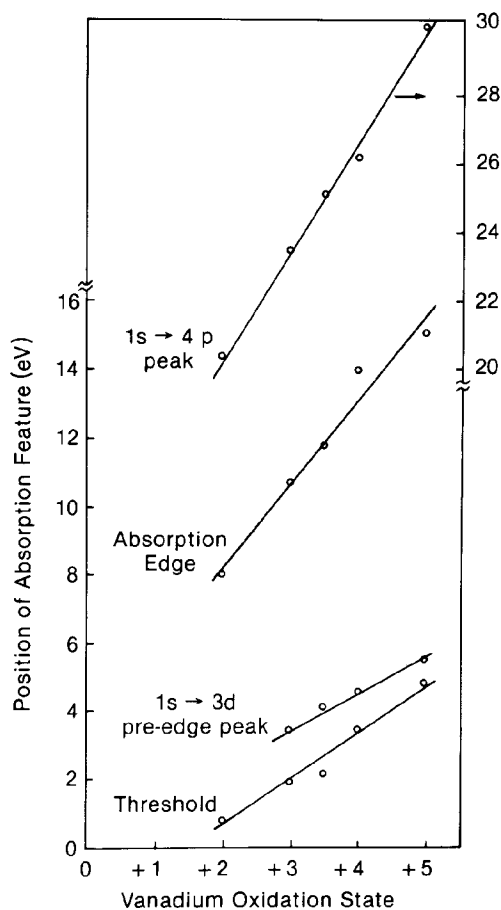
Fig. 13. Oxidation state *vs.* energy positions of various absorption features in the K-edge XANES spectra of vanadium in the various vanadium oxides shown in Fig. 12.

crease in the attractive potential of the nucleus on the 1s electron and a reduction in the repulsive core Coulomb interaction with all the other electrons in the compound. The full lines in Fig. 13 are least-squares fitted lines with slopes of 1.4 eV, 1.1 eV, 2.5 eV and 3.2 eV per valence increase for the threshold, the pre-edge peak, the absorption edge and the 1s → 4p transition respectively. The increase in slope merely reflects tighter binding of the inner 3d and 4s levels with respect to the outermost 4p levels which are more easily perturbed by valence change.

6. UNIQUE FEATURES OF EXTENDED X-RAY ABSORPTION FINE STRUCTURE

In this section we illustrate the unique features of EXAFS as a structural probe by way of an example. In Fig. 14(a) the EXAFS above the K edges of both iron and nickel in a b.c.c. Fe-Ni alloy containing 80 at.% Fe are shown. These were obtained in one experimental scan by first tuning the synchrotron radiation near the K absorption edge of iron at 7.11 keV, scanning the iron EXAFS over a 1000 eV range and continuing to scan another 1000 eV beyond the K edge of nickel to obtain its EXAFS. It should be noted that iron and nickel are separated by 2 units in atomic number, and yet their K absorption edges are far apart in energy so that the EXAFS of iron is not overlapped by the onset of the K absorption of nickel. This in turn means that structural information extracted from analyzing each EXAFS spectrum is atom specific in the sense that the central atom is defined; hence, the origin of each of the $\phi(r)$ is known. This clearly demonstrates atomic selectivity of the EXAFS technique for studying multi-atomic systems.

Using the data reduction procedure described in Section 4, the normalized EXAFS for nickel is obtained and plotted as χk *versus* k in Fig. 14(b). This is then Fourier transformed with respect to $\exp(2ikr)$ to obtain $\phi(r)$ which is shown in Fig. 14(c). The Fourier transform is dominated essentially by a strong radial structure peak above 2 Å, but higher coordination shells are also visible to 5-6 Å. The oscillations on the low r side of the first peak are due to termination errors of the transform and are not structural in origin. Compared with the transform shown in Fig. 9(c) for pure nickel which is f.c.c. and has 12 nearest neighbors, the transform pattern shown in Fig. 14(c) for nickel in the b.c.c. Fe-Ni alloy is quite different. The latter in fact is characteristic of a b.c.c. structure such as iron which has eight nearest neighbors [41]. This can also be seen directly in the raw spectra in Fig. 14(a) in that the Ni-Fe EXAFS pattern is isomorphic with that of iron and is a direct consequence of the alloying effect which results in structuring the nickel atoms in a b.c.c. lattice.

Finally, it is of interest to have a comparison of the EXAFS technique with conventional X-ray diffraction in order to select an appropriate tool for the particular need in material characterization. The comparison is given in Table 2. In summary, the unique features of EXAFS as a structural tool are (1)
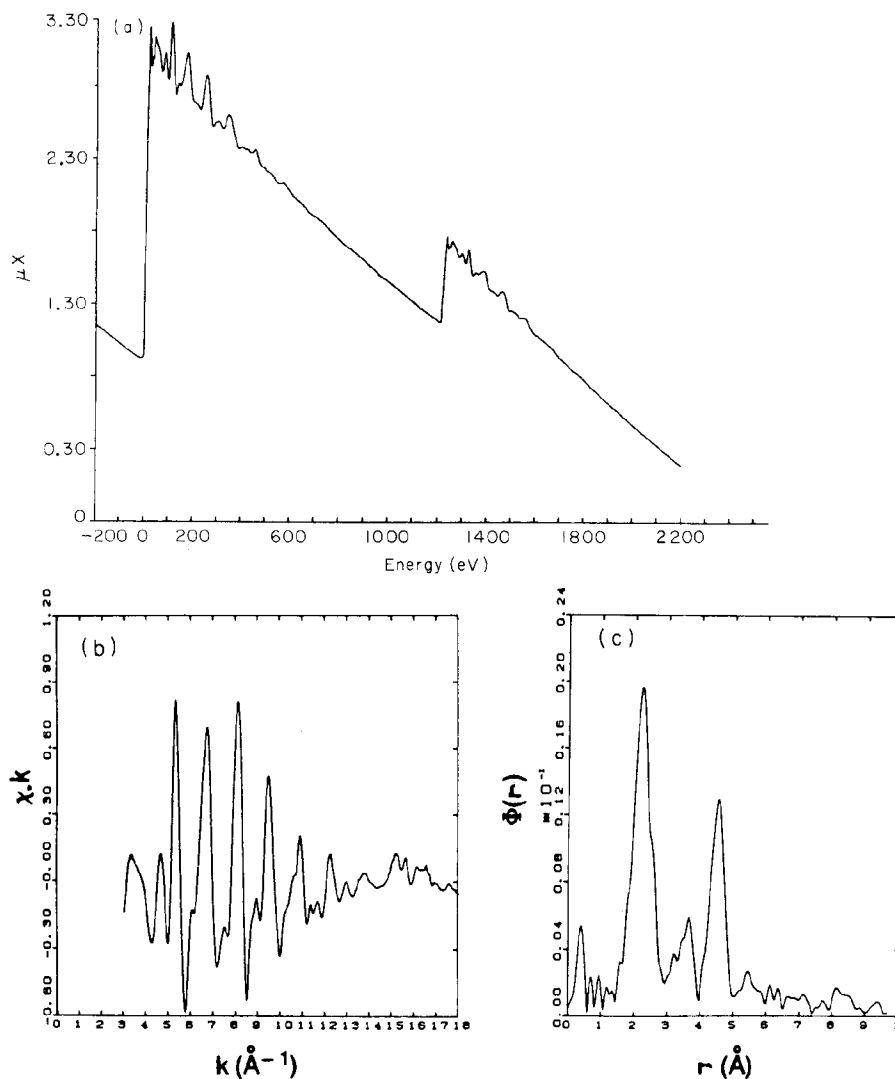
124

Fig. 14. B.c.c. Fe–Ni alloy containing 80 at.% Fe: (a) experimental EXAFS spectra above the K edges of iron and nickel; (b) normalized EXAFS plotted as χk vs. k in the nickel EXAFS; (c) Fourier transform of (b). The peaks on the low r side of the first main peak at 2.2 Å are spurious effects of the transform and are therefore nonphysical. It should be noted that this radial structure function for nickel in a b.c.c. environment is quite different from that for pure f.c.c. nickel shown in Fig. 9(c).

that it is element selective, (2) that it has a high sensitivity to short-range order, (3) that it is applicable to all states of matter in a dilute or bulk form and (4) that, when it is combined with XANES, it yields both electronic (chemical bonding) as well as atomic structure.

7. APPLICATIONS

The application of EXAFS to a variety of material characterization problems is rapidly evolving. To date, the most fully developed applications are toward the field of disordered systems, catalysis and biology. As the technique is being extended to other materials whether in different states or different configurations, new detection schemes are also developed to enable extraction of the EXAFS signal in a possible and more efficient way in terms of the signal-to-noise ratio. In this review, we shall not attempt to compile a comprehensive list of EXAFS experiments. Instead, we have abstracted a number of author-

TABLE 2

Extended X-ray absorption fine structure *versus* X-ray diffraction

	EXAFS	*X-ray diffraction*
r space range	Short, since $\chi(k) \approx 1/r^2$ and $\lambda \leqslant 10$ Å	Long
k space range	$0\,\text{Å}^{-1} < k < 50\,\text{Å}^{-1}$	$0\,\text{Å}^{-1} \leqslant q \leqslant 25\,\text{Å}^{-1}$
Selectivity	Atom specific	All atoms diffract
N_j	±10%	±1% or better
r_j	± 0.02 Å for first shell; ± 0.1 Å for second shell	0.001 Å
σ_j	Two-body average	One-body average
ϕ_j	Contains phase information	No phase
Material systems	All states of matter, bulk and dilute	Crystalline solids, bulk

itative reviews, both general and with special emphasis in various disciplines covering condensed matters, amorphous solids including metallic glasses, catalysts, biomolecules, chemistry, solution and geology. Also, newly developed detection schemes will be discussed so that the interested reader may be able to design the appropriate experimentation for his or her material systems of investigation.

7.1. General reviews

Reference 40 is an authoritative review on the basic principles and experimentation of EXAFS. Various applications are reviewed in decreasing length for disordered systems, biology, catalysis, metal–metal bonds in inorganic chemistry, intercalation systems, defects and impurities (mainly in metallurgical systems) and solutions. Surface EXAFS is also discussed.

The development of the EXAFS formalism in ref. 42 is rather mathematical and is difficult for the non-mathematically oriented reader to follow. In decreasing length, descriptions of the following applications are given: crystalline solids including elemental and simple binary compounds, superionic conductors, mixed valence materials, spin glasses, solid solutions (alloys) and A15 compounds; disordered solids; surface and absorbates on surfaces; liquids; catalysts. Biological materials are just briefly mentioned.

7.2. Biology

Reference 38 is devoted to a review of EXAFS and near-edge investigations of bio-

molecules studied up to 1978. These included rubredoxin, hemoglobin, cytochrome P-450 and chloroperoxidase, azurin, nitrogenase, cytochrome oxidase, hemocyanin, carbonic anhydrase and platinum complexes bound to deoxyribonucleic acid. The review was updated in 1981 [70] to include the blue copper proteins (stellacyanin and plastocyanin), xanthine oxidase and sulfite oxidase, ferritin and calcium binding proteins.

7.3. Catalysts

Reference 71 reviews the experimental technique of measuring EXAFS spectra of catalysts *in situ*. Systems discussed include dispersed metal catalysts, metal oxide catalysts and homogeneous catalysts of the Wilkinson type. Chemical information about the catalytic center as derived from the near-edge structure is also discussed.

7.4. Amorphous materials

Reference 41 is a review on the metal–metalloid type of glasses that were studied up to the end of 1979. The review has been expanded and updated twice by Gurman [72, 73] to include metal–metal type of glasses, chalcogenide glasses, oxide glasses, melts and solutions.

7.5. Geology

Finally the application of EXAFS to geology for characterizing the bonding and local atomic structure of specific atomic sites in minerals of geological importance is now emerging. This is evident in a symposium devoted to the

application of EXAFS and near-edge spectroscopy to geology and geochemistry held at the 1984 International Conference on EXAFS at Stanford [74].

8. OTHER DETECTION SCHEMES

It can be said that the modern EXAFS technique has been built on two major milestones in the early 1970s: (i) the elucidation of the basic physics of the phenomenon in terms of the single-scattering formalism and Fourier transform of the experimental signal to yield quantitative structural information [15] and (ii) the availability of intense well-collimated synchrotron radiation in the X-ray region [25, 26] as a light source for high quality and fast acquisition of experimental spectra. Since then, a number of detection schemes have been developed in order to explore the application of EXAFS to other materials in various states and configurations that are not amenable to conventional transmission measurement. These schemes include electron detection in ultrahigh vacuum for surface structure studies (of adsorbates) [75], fluorescence

for dilute systems (biomolecules) and trace impurities [33], dispersive EXAFS for kinetic studies at a time scale of under a minute [76, 77], double fluorescence for discriminating between dilute impurities in a slightly lower Z matrix [78], reflection EXAFS for subsurface (buried interface) characterization [79] and electron detection in non-vacuum conditions [80]. Table 3 summarizes each scheme and outlines their application.

9. CONCLUDING REMARKS

It is clear that, by virtue of the fact that EXAFS is an atom-specific and local structural tool, it provides the chemist, the physicist, the biologist, the materials scientist, the geologist and the metallurgist with an optional and oftentimes unique tool for characterizing materials. In combination with the near-edge structure, this mode of X-ray absorption spectroscopy is a very powerful tool for elucidating both the atomic and the electronic structure of matter. However, the practitioner of this technique must bear in mind that considerable care has to be taken to interpret data of an elemental species existing in more than one structural and/or chemical environment, since the EXAFS signal from each site will be collected over the same energy range of the measured spectrum.

TABLE 3

Other extended X-ray absorption fine structure detection schemes

Scheme	Year	Remarks
Fluorescence	1977	Uses fluorescent X-ray photons to monitor μx of dilute species
Surface EXAFS	1978	Uses Auger electrons to monitor μx of surface atoms
Dispersive	1982	Rapid scan for kinetic studies
Double fluorescence	1983	For heavy impurities in slightly lower Z matrix
Reflection EXAFS	1984	Probes for buried interfaces
Electron detection	1984	Applicable for use at atmospheric pressure, thus avoiding ultrahigh vacuum conditions

REFERENCES

1 F. W. Lytle, in J. A. Prins (ed.), *Physics of Non-crystalline Solids*, North-Holland, Amsterdam, 1965, pp. 12–25.
2 H. Fricke, *Phys. Rev., 16* (1920) 202.
3 G. Hertz, *Phys. Z., 21* (1920) 630; *Z. Phys., 3* (1920) 19.
4 R. De L. Kronig, *Z. Phys., 70* (1921) 317; *75* (1932) 191.
5 T. Hayashi, *Sci. Rep. Tohoku Univ., 33* (1949) 123, 183.
6 L. V. Azaroff, *Rev. Mod. Phys., 35* (1963) 1012.
7 E. A. Stern, *Phys. Rev. B, 10* (1974) 3027.
8 J. D. Hanawalt, *Phys. Rev., 37* (1931) 715.
9 B. M. Kincaid and P. Eisenberger, *Phys. Rev. Lett., 34* (1975) 1361.
10 B. M. Kincaid, *Ph.D. Thesis*, Stanford University, 1975.
11 R. A. Van Nordstrand, in V. D. Frechette (ed.), *Non-crystalline Solids*, Wiley, New York, 1960, p. 108.
12 W. F. Nelson, I. Siegel and R. W. Wagner, *Phys. Rev., 127* (1962) 2025.

127

13 F. W. Lytle, D. E. Sayers and E. A. Stern, The history and modern practice of EXAFS spectroscopy. In C. Bonnelle and C. Mande (eds.), Advances in X-ray Spectroscopy, Pergamon, Oxford, 1982, Chapter 16, p. 267.

14 D. E. Sayers, F. W. Lytle and E. A. Stern, Adv. X-ray Anal., 13 (1970) 248.

15 D. E. Sayers, E. A. Stern and F. W. Lytle, Phys. Rev. Lett., 27 (1971) 1204.

16 H. Bethe and E. Salpeter, Quantum Mechanics of One- and Two-electron Systems, Springer, Berlin, 1959, Sections 59, 69.

17 W. H. McMaster, N. Nerr del Grande, J. H. Mallett and J. H. Hubbell, Compilation of X-ray cross sections, Rep. UCRL-50/74, Section 2, Rev. 1, 1969 (Lawrence Radiation Laboratory, University of California).

18 C. A. Ashley and S. Doniach, Phys. Rev. B, 11 (1975) 1279.

19 P. A. Lee and J. B. Pendry, Phys. Rev. B, 11 (1975) 2795.

20 P. A. Lee and G. Beni, Phys. Rev. B, 15 (1977) 2862.

21 R. F. Pettifer and P. W. McMillan, Philos. Mag., 35 (1977) 871.

22 F. Jona, Surf. Sci., 68 (1977) 204.

23 A. Bianconi, Appl. Surf. Sci., 6 (1980) 392.

24 B. K. Teo, J. Am. Chem. Soc., 103 (1981) 3990.

25 A. D. Baer, R. Gaxiola, A. Golde, F. Johnson, B. Salsburg, H. Winick, M. Baldwin, N. Dean, J. Harris, E. Hoyt, B. Humphrey, J. Jurow, R. Melen, J. Miljan and G. Warren, IEEE Trans. Nucl. Sci., 22 (1975) 1794.

26 S. Doniach, I. Lindau, W. R. Spicer and H. Winick, J. Vac. Sci. Technol., 12 (1975) 1123.

27 J. Schwinger, Phys. Rev., 75 (1949) 1912.

28 H. Winick, in H. Winick and S. Doniach (eds.), Synchrotron Radiation Research, Plenum, New York, 1980, Chapter 2, p. 11.

29 F. R. Elder, R. V. Langmuir and H. D. Pollock, Phys. Rev., 74 (1948) 52.

30 H. C. Pollock, Am. J. Phys., 51 (3) (1983) 278.

31 R. F. Pettifer, Ph.D. Thesis, University of Warwick, 1978.

32 S. H. Hunter, Ph.D. Thesis, Stanford University, 1977.

33 J. Jaklevic, J. A. Kirby, M. P. Klein, A. S. Robertson, G. S. Brown and P. Eisenberger, Solid State Commun., 23 (1977) 679.

34 E. A. Stern and S. M. Heald, Rev. Sci. Instrum., 50 (12) (1979) 1579.

35 J. B. Hasting, P. Eisenberger, B. Lengeler and M. C. Perlman, Phys. Rev. Lett., 43 (1979) 1807.

36 M. Marcus, L. S. Powers, A. R. Storm, B. M. Kincaid and B. Chance, Rev. Sci. Instrum., 51 (1980) 1023.

37 F. W. Lytle, D. E. Sayers and E. A. Stern, Phys. Rev. B, 11 (1975) 4825.

38 S. P. Cramer and K. O. Hodgson, Prog. Inorg. Chem., 25 (1979) 1.

39 G. S. Brown, in H. Winick and S. Doniach (eds.), Synchrotron Radiation Research, Plenum, New York, 1980, Chapters 10, 11.

40 P. A. Lee, P. H. Citrin, P. Eisenberger and B. M. Kincaid, Rev. Mod. Phys., 53 (4) (1981) 769.

41 J. Wong, Top. Appl. Phys., 46 (1981), Chapter 4.

42 T. M. Hayes and J. B. Boyce, Solid State Phys., 37 (1982) 173.

43 E. A. Stern and S. M. Heald, in E. E. Koch (ed.), Handbook on Synchrotron Radiation, Vol. 1, North-Holland, Amsterdam, 1983, Chapter 10.

44 A. L. Robinson, Science, 205 (1979) 1367.

45 G. S. Knapp, H. Chen and T. E. Klippert, Rev. Sci. Instrum., 49 (1978) 1658.

46 G. G. Cohen, D. A. Fischer, J. Colbert and N. J. Shevchik, Rev. Sci. Instrum., 51 (3) (1980) 273.

47 A. Williams, Rev. Sci. Instrum., 54 (2) (1983) 193.

48 W. Thulke, R. Haensel and P. Rabe, Rev. Sci. Instrum., 54 (3) (1983) 277.

49 H. Winick, in H. Winick and S. Doniach (eds.), Synchrotron Radiation Research, Plenum, New York, 1980, Chapter 3.

50 E. A. Stern, D. E. Sayers and F. W. Lytle, Phys. Rev. B, 11 (1975) 4836.

51 B. Lengeler and P. Eisenberger, Phys. Rev. B, 21 (1980) 4507.

52 B. K. Teo and P. A. Lee, J. Am. Chem. Soc., 101 (1979) 2815.

53 C. Bingham, M. D. Godfrey and J. W. Turkey, IEEE Trans. Audio and Electroacoust., 15 (2) (1967) 58.

54 J. Wong, E. F. Koch, C. I. Hejna and M. F. Garbauskas, J. Appl. Phys., 58 (9) (1985) 3388.

55 S. Rundquist, Acta Chem. Scand., 12 (1958) 658.

56 P. H. Citrin, P. Eisenberger and B. M. Kincaid, Phys. Rev. Lett., 36 (1976) 1346.

57 B. K. Teo, P. Eisenberger, J. Reed, J. K. Barton and S. J. Lippard, J. Am. Chem. Soc., 100 (1978) 3225.

58 S. P. Cramer, K. O. Hodgson, E. I. Stiefel and W. R. Newton, J. Am. Chem. Soc., 100 (1978) 2748.

59 G. H. Via, J. H. Sinfelt and F. W. Lytle, J. Chem. Phys., 71 (1979) 690.

60 J. Wong and H. H. Lieberman, Phys. Rev. B, 29 (1984) 651.

61 K. J. Rao, J. Wong and M. J. Weber, J. Chem. Phys., 78 (1983) 6228.

62 J. H. Sinfelt, G. H. Via and F. W. Lytle, J. Chem. Phys., 72 (1980) 4832.

63 M. C. Srivastava and H. L. Nigam, Coord. Chem. Rev., 9 (1972) 275.

64 J. Wong, F. W. Lytle, R. P. Messmer and D. H. Maylotte, Phys. Rev. B, 30 (1984) 5596.

65 R. G. Shulman, Y. Yafet, P. Eisenberger and W. E. Blumberg, Proc. Natl. Acad. Sci. U.S.A., 73 (1976) 1384.

66 J. L. Dehmer, J. Chem. Phys., 56 (1972) 4496.

67 P. J. Durham, J. B. Pendry and C. H. Hodges, Solid State Commun., 38 (1981) 159.

68 F. W. Kutzler, C. R. Natoli, D. K. Misemer, S. Doniad and K. O. Hodgson, J. Chem. Phys., 73 (1980) 3274.

69 V. Kunzl, Collect. Trav. Cjim. Techecolovaquie, 4 (1932) 213.

70 S. Doniach, P. Eisenberger and K. O. Hodgson, in H. Winick and S. Doniach (eds.), Synchrotron Radiation Research, Plenum, New York, 1980, Chapter 13, pp. 425-458.

71 F. W. Lytle, G. H. Via and J. H. Sinfelt in H.

Winick and S. Doniach (eds.), *Synchrotron Radiation Research*, Plenum, New York, 1981, Chapter 12, pp. 401–424.

72 S. J. Gurman, *J. Mater. Sci., 17* (1982) 1541.

73 S. J. Gurman, EXAFS studies of amorphous materials, in R. W. Joyner (ed.), *Extended X-ray Absorption Fine Structure*, Plenum, London, 1985, Chapter 6.

74 K. O. Hodgson, B. Hedman and J. E. Penner-Hahn (eds.), *Proc. Int. Conf. on Extended X-ray Absorption Fine Structure*, Part VII, *Geology and Geochemistry of EXAFS and Near-edge Structure III*, Springer, Berlin, 1984, pp. 336–390.

75 P. H. Citrin, P. Eisenberger and R. C. Hewitt, *Phys. Rev. Lett., 41* (1978) 309.

76 A. M. Flank, A. Fontain, A. Jucha, M. Lommnier and C. Williams, *J. Phys. (Paris), Lett., 43* (1982) L315.

77 R. P. Phizackerley, Z. U. Rek, G. B. Stephenson, S. D. Conradson, K. O. Hodgson, T. Matsushita and H. Oyanagi, *J. Appl. Crystallogr., 16* (1983) 220.

78 J. Wong and K. J. Rao, *Solid State Commun., 45* (9) (1983) 853.

79 S. M. Heald, E. Keller and E. A. Stern, *Phys. Lett. A, 103* (1984) 155.

80 M. E. Kordeseh and R. W. Hoffman, *Phys. Rev. B, 29* (1984) 491.